UNIVERSITÀ DEGLI STUDI DI PADOVA

Dipartimento di Fisica e Astronomia "Galileo Galilei"

Corso di Laurea in Fisica

Tesi di Laurea

Heavy ion fusion reactions far below barrier and their astrophysical implications

Relatore

Prof. Giovanna Montagnoli

Correlatore

Prof. Alberto Stefanini

Laureando

Leonardo Palombini

Abstract

Fusion reactions between heavy nuclei have been a hot topic in nuclear physics since the first experiments took place in the 80s: amidst the plethora of subjects involved, the study of low energy collision dynamics is one of the most prolific and interesting fields of study, especially because of its tight connection with stellar thermonuclear processes. In this context, the experimental work presented in this thesis aims to extend the current knowledge about fusion between medium-light nuclei at energies far below the Coulomb barrier, particularly looking for the hindrance phenomenon. The investigation of medium-light systems helps understanding the behaviour of the lighter ones, especially the processes of carbon and oxygen burning in the late stages of star evolution. This thesis work consists of the experimental study of such medium-light systems, involving ^{12}C and heavier nuclei like $^{24\text{-}26}$Mg and ^{28}Si, more specifically the fusion reaction ^{12}C $+^{26}$ Mg. The measured cross sections are discussed and compared to the predictions of current theoretical models.

Structure of the work: at first, an overview of the theoretical models adopted is provided; then, a description of experimental setup and computational instruments used; data analysis, results and conclusions will end the work.

Contents

1 Theoretical background

1.1 Introduction

Heavy ion fusion is the reaction that gets two colliding nuclei, heavier than alpha particles, to bind together and create a composite nucleus. While getting close to each other, ions are influenced by two opposite forces: Coulomb repulsion, due to the positive charge of their protons, and nuclear force, that tends to attract nucleons together. As it's known, the latter is a short range interaction: that means that the two nuclei need to have enough kinetic energy to "climb" the electrostatic potential and get close enough, in order for fusion to occur. So, from a classical mechanics point of view, all ions with less energy than the Coulomb potential barrier shall simply bounce back. However, in the realm of quantum mechanics, there's a certain probability that these nuclei will penetrate the Coulomb barrier, due to the tunneling phenomenon. If it wasn't true, most of the thermonuclear reactions in stars wouldn't take place, since they work in the classically forbidden energy region.

1.2 Models for general heavy-ion fusion

The purpose of this section is to illustrate the standard models used to analyze the process of heavy-ion fusion, focusing on the sub-barrier energy regimen. During the last 60 years, theoretical and computational methods evolved together with experimental evidences: for this reason, models are described in a progression of increasing completeness and accuracy.

1.2.1 Simple ion-ion potential model

The first approach to get a description of this phenomenon is to assume both projectile and target nuclei to be structureless and spherical-symmetric. In this approximation, a simple central potential, accounting for nuclear and Coulomb interactions, can be employed [1][2]:

$$V(r) = V_N(r) + V_c(r) \tag{1}$$

where $V_c(r) = \frac{Z_P Z_T e^2}{4\pi\epsilon_0 r}$ is the standard Coulomb potential (valid in regions of non-overlapping nuclei) and V_N is usually a phenomenological potential. For example, the Wood-Saxon potential is widely used [1][3]:

$$V_N(r) = -\frac{V_0}{1 + exp[(r - R_0)/a]} \tag{2}$$

where V_0 is well's depth, R_0 can be regarded as the well's radius (in this case, it's the sum of the radii of the colliding nuclei) and a is the "diffuseness". Another way to obtain V_N is the so-called double-folding procedure [1]:

$$V_N(r) = \int d\mathbf{r_1} d\mathbf{r_2} v_n(\mathbf{r_1} - \mathbf{r_2} - \mathbf{r}) \rho_P(\mathbf{r_1}) \rho_T(\mathbf{r_2}) \tag{3}$$

where $v_n(\mathbf{r_1} - \mathbf{r_2} - \mathbf{r})$ is the nucleon-nucleon interaction.

Sometimes, a purely phenomenological imaginary part is added to standard $V(r)$ [1][2][3], in order to account for the absorbed incident flux due to fusion reaction. This $V_{OM} = V(r) - iW(r)$ is often regarded as the *optical potential* [4]: its use isn't mandatory, but it's a consequence of the choice of the boundary conditions (see later).

The global Hamiltonian for this system, in the CM frame of reference, is:

$$H = -\frac{\hbar^2}{2\mu}\nabla^2 + V(r) + (-iW(r)) \tag{4}$$

which, in the more natural spherical coordinates (r, θ, ϕ), is written, in the reduced form (i.e. fixing the angular momentum value) [1]:

$$H = -\frac{\hbar^2}{2\mu} r^{-2} \frac{\partial}{\partial r}\left(r^2 \frac{\partial}{\partial r}\right) + \frac{\hbar^2 l(l+1)}{2\mu r^2} + V(r) + (-iW(r)) = T_r + V_{eff}(r) + (-iW(r)) \tag{5}$$

where l is the quantum orbital number, and V_{eff} is the effective potential accounting for the centrifugal term. It's easy to see that this term, for higher values of l, decreases the depth of potential's "pocket" until the potential itself becomes purely repulsive:
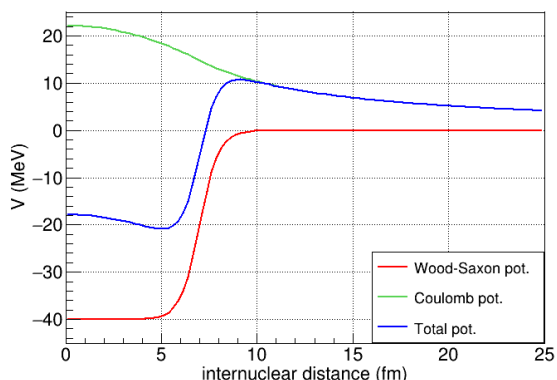
(a) Total internuclear potential $V(r)$.
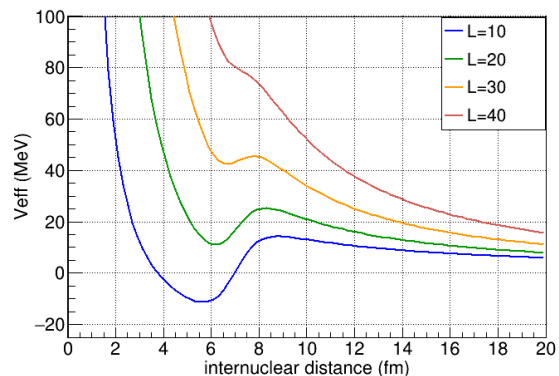
(b) Effective potential $V_{eff}(r)$, with different values of l.

Figure 1

the value l_{crit} where this happens will be useful later, because it imposes an upper limit to the configurations that allow the fusion reaction.

We get to solve the usual Schrödinger equation $(H - E)\psi_l = 0$. A standard choice for the boundary conditions is [1][3]:

$$\begin{cases} \psi_l(r) \sim r^{l+1} & r \to 0 \\ \psi_l(r) \sim H_l^{(-)}(kr) - S_l H_l^{(+)}(kr) & r \to \infty \end{cases} \tag{6}$$

where $H_l^{(-)}$ and $H_l^{(+)}$ are respectively the incoming and outgoing Coulomb wavefunction, S_l is the nuclear scattering matrix and $k = \sqrt{\frac{2\mu E}{\hbar^2}}$ is the usual wavenumber for E (energy in the CM).

From this calculations, we'd like to extract the cross section for the fusion reaction, whose general formula is [1][5][6]:

$$\sigma_{fus,l} = \frac{\pi}{k^2}(2l+1)T_l(E) \tag{7}$$

for the lth partial wave, where T_l is the associated transmission coefficient.

In this case, fusion cross section (zero-spin nuclei) is calculated from (7), using $T_l = 1 - |S_l^2|$, as:

$$\sigma_{fus} = \frac{\pi}{k^2}\sum_{l=0}^{l_{crit}}(2l+1)(1 - |S_l|^2) \tag{8}$$

Another possibility is to apply the IWBC (Incoming Wave Boundary Conditions) [1]. This choice allows to avoid using the imaginary potential, under the further assumption of "strong absorption" (the incoming flux doesn't bounce back) [3]. The new condition is:

$$\psi_l(r) = \sqrt{\frac{k}{k_l(r)}}\, T_l\, exp\left[-i\int_{r_{abs}}^r k_l(r')dr'\right] \qquad r < r_{abs} \tag{9}$$

where $k_l(r) = \sqrt{\frac{2\mu}{\hbar^2}(E - V_{eff}(r))}$ is the local wave number, r_{abs} is the inter-nuclear distance where absorption starts, and $\tilde{T}_l$ is the transmission coefficient. Here, the formula for cross section is computed as before.

Since the actual analytical solution of this equations may be quite laborious (sometimes impossible), a number of approximations and computational approaches has been developed. One of the most used was proposed by Hill and Wheeler (mid-50s) [7]: the Coulomb barrier is approximated by an inverted harmonic potential (inverted parabola) of the form [6][7]

$$V_{eff}(r) \approx \frac{1}{2}V''(r = R_{B,l})(r - R_{B,l}) \tag{10}$$

Defining $\omega_{B,l} = \sqrt{-\frac{V''_{eff}(r=R_{B,l})}{\mu}}$, calculations for tunneling probabilities yield this formula for the transmission coefficent [2][6]:

$$T_l = \left[1 + exp\left[\frac{2\pi}{\hbar\omega_{B,l}}(V_{eff}(r = R_{B,l}) - E)\right]\right]^{-1} \tag{11}$$

which can be substituted in (7), and finally, replacing the sum of l with an integration (assumption of large number of possible $l \le l_{crit}$) [2]:

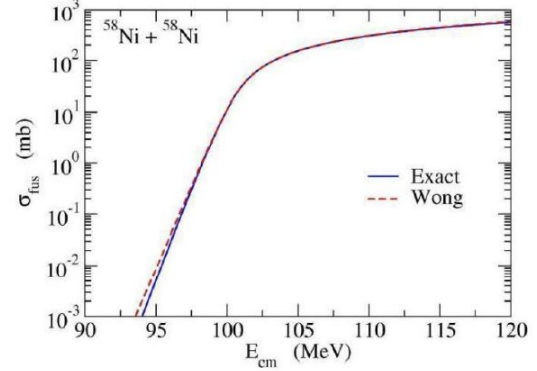$$\sigma_{fus}(E) = \frac{\hbar\omega_B}{2E}R_B^2 ln\left[1 + exp\left(\frac{2\pi}{\hbar\omega_B}(E - V_B)\right)\right] \tag{12}$$

considering that, for $l \le l_{crit}$, R_B and ω_B are substantially independent from l. This is sometimes called *Wong formula*.

3

Comparing this result with the one obtained by numerical solution of the exact model, for a given system, an excellent consistency is verified.
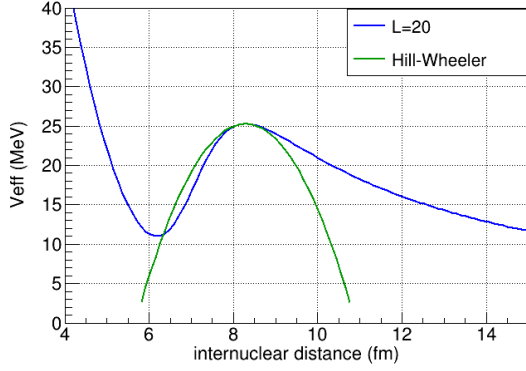

(a) Parabolic approximation of V_{eff} barrier.

(b) Cross section prediction comparison using exact potential *vs* Wong formula, for the reaction $^{58}\text{Ni} + ^{58}\text{Ni}$. Courtesy of ref. [2].
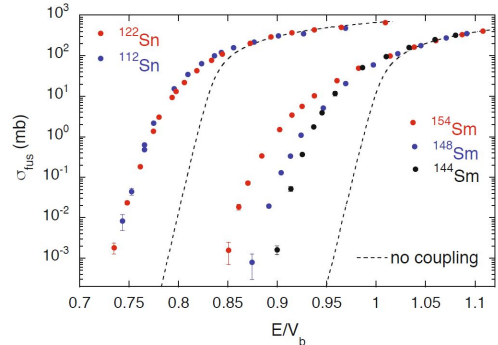
Figure 2

1.2.2 Potential model: comparison with experimental data

This model is good at predicting σ_{fus} for energies above V_B, but largely underpredicts it in many systems when exploring the sub-barrier energy region [1][2][3]. Other potential parametrizations (ex. Akyuz-Winther pot., ...) brought similar results.
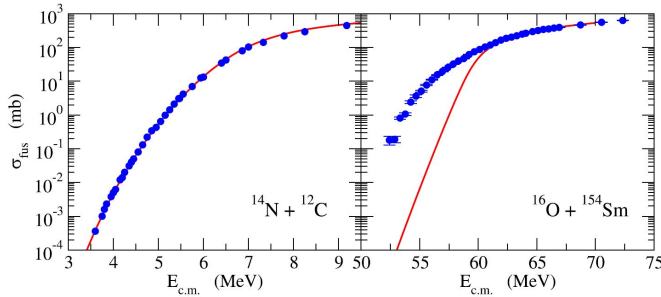
(a) Excitation functions for $^{14}\text{N}+^{12}\text{C}$ and $^{16}\text{O}+^{154}\text{Sm}$, taken from ref. [1]: the first follows potential model's predictions, the latter shows a large positive difference.

(b) Comparison of reactions between ^{40}Ar and $^{112,122}\text{Sn}$, $^{144,148,154}\text{Sm}$. E_{CM} is normalized to barrier height. Taken from ref. [8].

Figure 3

This phenomenon was called *enhancement*. It appears with different magnitudes (spanning up to several orders of mag.) or sometimes not at all, presenting clear differences also between "neighbouring" systems: this suggests a substantial dependence on nuclear structure, low-level excitations, transfer channels and internal degrees of freedom in general [2][8]. That brought to the development of the Coupled Channels model.

1.2.3 Coupled Channels model

This model was developed to account for internal degrees of freedom (DoF), and does so defining a set of generalized coordinates $(\bar{r}, \xi)$, where ξ represents internal DoF. The new Hamiltonian is [1][2][8]:

$$H_{CC} = T_r + V_{eff}(r) + H_0(\xi) + V_C(\bar{r}, \xi) = H_r + H_0(\xi) + V_C(\bar{r}, \xi) \tag{13}$$

4

where $H_0(\xi)$ is the hamiltonian relative to the nuclear structure and $V_C(\overline{r}, \xi)$ is the potential that couples nuclei's relative motion to the reaction channels.

Here a simplified version of the involved calculations, proposed by [2] and [8], will be shown: in real applications, the model is numerically implemented in a computer program called `CCfull` [9]. Nevertheless, this treatment effectively highlights the influence of coupling in fusion dynamics.

The Schrödinger equation is, as always:

$$(H_{CC} - E)\Psi(\overline{r}, \xi) = 0 \tag{14}$$

The total wavefunction can be decomposed as:

$$\Psi(\overline{r}, \xi) = \sum_k \psi_k(\overline{r})\phi_k(\xi) \tag{15}$$

where $\phi_k(\xi)$ are the eigenfuctions of $H_0(\xi)$, satisfying $H_0(\xi)\phi_k(\xi) = \epsilon_k\phi_k(\xi)$. In the next passages, Dirac bra-ket notation will be used for readability. (14) can be rewritten using (15) and projected onto ϕ_k in the following way:

$$\langle\phi_k| (H_{CC} - E) \sum_{k'} |\psi_{k'}\rangle |\phi_{k'}\rangle = 0 \qquad \rightarrow \qquad \sum_{k'} |\psi_{k'}\rangle \langle\phi_k| H_{CC} - E |\phi_{k'}\rangle = 0 \tag{16}$$

Expanding H_{CC} and computing the individual terms:

$$\sum_{k'}(\delta_{kk'}(H_r + \epsilon_{k'} - E) + \langle\phi_k| V_C |\phi_{k'}\rangle)|\psi_{k'}\rangle \;=\; (H_r - E)|\psi_k\rangle + \sum_{k'} M_{kk'}|\psi_{k'}\rangle = 0 \tag{17}$$

where $M_{kk'} = \delta_{kk'}\epsilon_{k'} + \langle\phi_k| V_C |\phi_{k'}\rangle$. Considering the case of a factorizable V_C [8]:

$$\langle\phi_k| V_C |\phi_{k'}\rangle = F(r) \langle\phi_k| G(\xi) |\phi_{k'}\rangle \approx F_0 G_{kk'} \tag{18}$$

approximating the form factor F(r) to a constant. (18) can be substituted in the expression for M, which can now be diagonalized:

$$(U \, M \, U^\dagger)_{kk'} = \lambda_{k'}\delta_{kk'} \tag{19}$$

where U is the diagonalizing unitary transformation and $\lambda_{k'}$ are the eigenvalues of M. By accordingly transforming the wavefunctions, i.e. defining $|Y_k\rangle = \sum_{k'} U_{kk'}\psi_{k'}$, the uncoupled equation is found [8]:

$$(H_r + \lambda_k - E)Y_k(r) = 0 \tag{20}$$

This is solved in the same way as (5) from the potential model, with an adequate choice of boundary conditions and Coulomb barrier.

Finally, the expressions for transmission coefficient and for fusion cross section are:

$$T_{CC,l}(E) = \sum_k |U_{ki}|^2 T_l(E, V_{eff}(R_{B,l}) + \lambda_k) \quad \rightarrow \quad \sigma_{fus} = \frac{\pi}{k^2} \sum_l (2l + 1)T_{CC,l}(E) \tag{21}$$

where $|U_{ki}|^2 = |\langle\phi_k|\phi_i\rangle|^2$ is the overlap between entrance (i) channel's state and k-th channel's one. The term $T_l(E, V_{eff}(R_{B,l}) + \lambda_k)$ is evaluated like (11). Now, however, the barrier is "split" in a number of barriers, one for each channel, of different heights $V_{eff} + \lambda_k$, thus making up a *barrier distribution*: each channel will then have its own $\sigma_{fus,k}$, and the total cross section will be a weighted average of these contributions [8]. For a lot of systems, this causes a lowering of the total barrier "perceived" by the nuclei, and enhances the cross section.

1.2.4 CC model: comparison with experimental data

This model was able to describe the behavior of numerous systems at energies below the Coulomb barrier, and helped researchers extract new information about nuclei's internal structures.
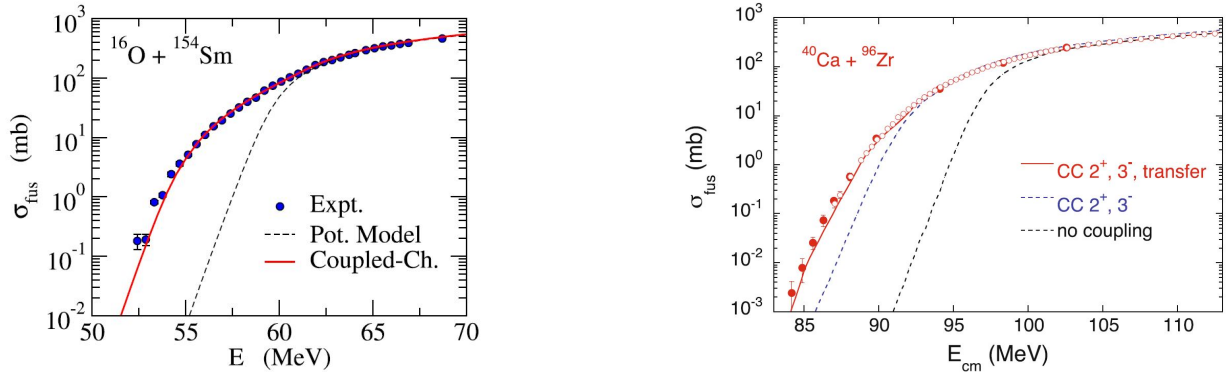
(a) Coupled Channels predictions nicely describe the excitation function of ^{16}O + ^{154}Sm. Taken from ref. [3].

(b) CC predictions using different couplings, for ^{40}Ca + ^{96}Zr. Taken from ref. [8].

Figure 4

The turning point came in 2002: Jiang et al.[11] found an unexpectedly fast decrease of σ_{fus} while studying the reaction ^{60}Ni+^{89}Y at extreme sub-barrier energy.
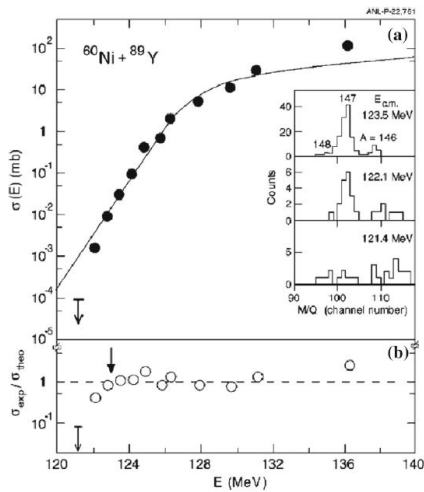

Figure 5: In this plot, taken from ref. [11], the excitation function mostly follows CC predictions. However, the two lowest-energy data points start showing a visible downward deviation, with the last one being at least one order of magnitude smaller than expected (its symbol represents an upper limit). Note that the involved values of cross section reach the sub-μb region.

This phenomenon was called *fusion hindrance* and, together with the improvement of low-energy measurements, was found to affect a variety of systems. The presence/absence and magnitude of hindrance, its causes and its consequences are still a current topic in nuclear physics debate. Some hypotheses have been developed to explain this particular behaviour.

1.2.5 Model hypotheses for fusion hindrance

One possible explanation is summed up in the so-called **sudden model**: when the two nuclei get in contact, the reaction is assumed to take place so suddenly (with respect to the variation of internal coordinates ξ) that the density in the overlapping region is doubled [3][5]. This leads to the formation of a further repulsive term in $V_{eff}(r)$ for $r \to 0$, due to the "incompressibility" of nuclear matter: microscopically, this behaviour is suggested to be a direct consequence of Pauli repulsion between nucleons [3]. The final effect is to decrease the depth of potential's pocket, so lowering the upper limit l_{crit} for the partial waves that contribute to fusion (see (5)) and, in fact, hindering the reaction [5].

Another hypothesis is offered by the **adiabatic model**. In contrast to the previous model, nuclei are assumed to smoothly merge into a one-body system: this causes the CC potential to adiabatically (i.e. minimizing energy at every step) and smoothly reshape in a mono-nucleus potential. Since this potential already accounts for internal excitations and optimizes intra-nuclei configurations [5], these channels don't take part to coupling effects anymore, effectively damping them and hindering fusion [3]. *De facto*, hindrance is viewed simply as gradual inhibition of coupling.
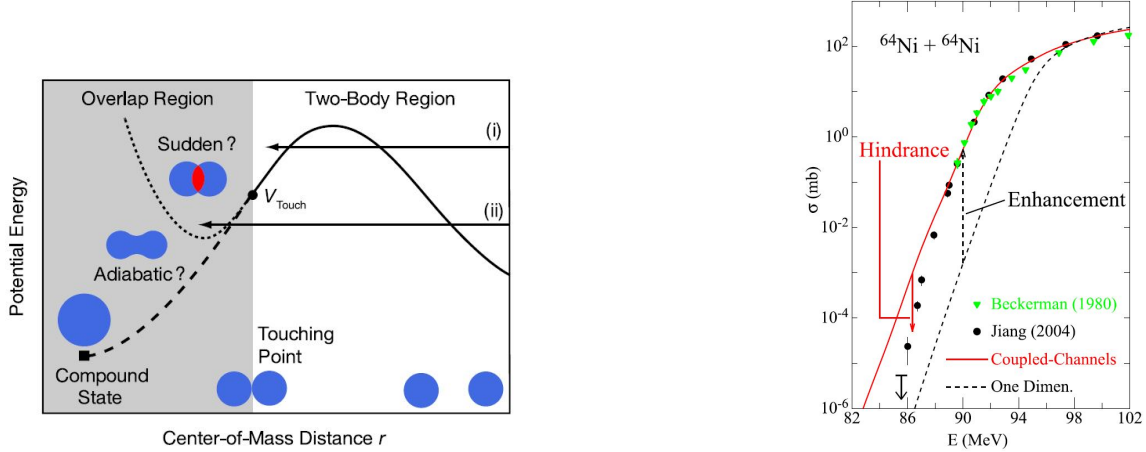
(a) Visual representation of the two theorized models for fusion hindrance, made by *T. Ichikawa, Phys. Rev. C 92, 064604 (2015)*. Picture taken from ref. [3].

(b) Clear example of excitation function where both enhancement and hindrance are visible, taken from ref. [3].

Figure 6

At present, both models equally describe experimental data down to the limits of instrumental capabilities. To be able to distinguish between them, it will be necessary to investigate even lower energy regions, or to measure other observables instead of σ_{fus} (e.g. the distribution of angular momenta involved in the fusion process).

Fusion hindrance will be the main topic of this experimental work.

1.3   Clues of hindrance in experimental data

As seen before, fusion hindrance leaves a sign of its presence in the excitation function (frequent synonym for the plot $\sigma_{fus}(E)$ vs E), by making it drop quicker than CC prediction. However, depending on the magnitude of the phenomenon, this behaviour can be sometimes difficult to spot or, in general, researchers may need more information than the bare cross section, in order to make better analyses. The most used derived quantities are [8]:

- **logarithmic derivative L(E)**

$$L(E) = \frac{\mathrm{d}[\ln(E\sigma(E))]}{\mathrm{d}E} = \frac{1}{E\sigma(E)} \frac{\mathrm{d}[E\sigma(E)]}{\mathrm{d}E} \tag{22}$$

- **astrophysical S factor S(E)**

$$S(E) = E\sigma(E)\,exp[2\pi\eta] \quad , \qquad \eta = \frac{Z_P Z_T e^2}{\hbar v} \tag{23}$$

where v is the beam velocity, and η is called *Sommerfeld parameter*.

Despite being mostly used to determine reaction rates in stars, the latter exhibits a particular behaviour when measured far below the barrier: experiments have shown that, in a number of systems, $S(E)$ develops a visible maximum at about the same energy where hindrance starts to become significant. For this reason, researchers often regard this point, E_H, as a threshold for hindrance.

7

1.3.1 S factor maximum at hindrance threshold

The deep physical meaning of the presence of a maximum of $S(E)$ closely related to hindrance phenomena is still a matter of debate. However, a simple algebraic argument is enough to give an *a posteriori* explanation.

Differentiating $S(E)$ (23) and using $v = (2E/m)^{\frac{1}{2}}$, the stationary-point condition is obtained:

$$\frac{\mathrm{d}S(E)}{\mathrm{d}E} = \left(\frac{\mathrm{d}[E\sigma(E)]}{\mathrm{d}E} - \pi\sigma(E) \right) exp[2\pi\eta] = S(E) \left(L(E) - \frac{\pi\eta}{E} \right) \overset{!}{=} 0 \qquad (24)$$

The first term, $L(E)$, accounts for the variation of cross section with E, and the second, $\frac{\pi\eta}{E}$, originates from Coulomb interaction and simply goes as $\propto \frac{1}{E}$. Around and above barrier, the latter usually dominates and the slope is negative. At lower energies they come closer to each other and, if hindrance occurs, the higher steepness of the excitation function makes $L(E)$ rise quicker: if this reaches the value $L_{CS} = \frac{\pi\eta}{E}$, a maximum of $S(E)$ shows up [12].
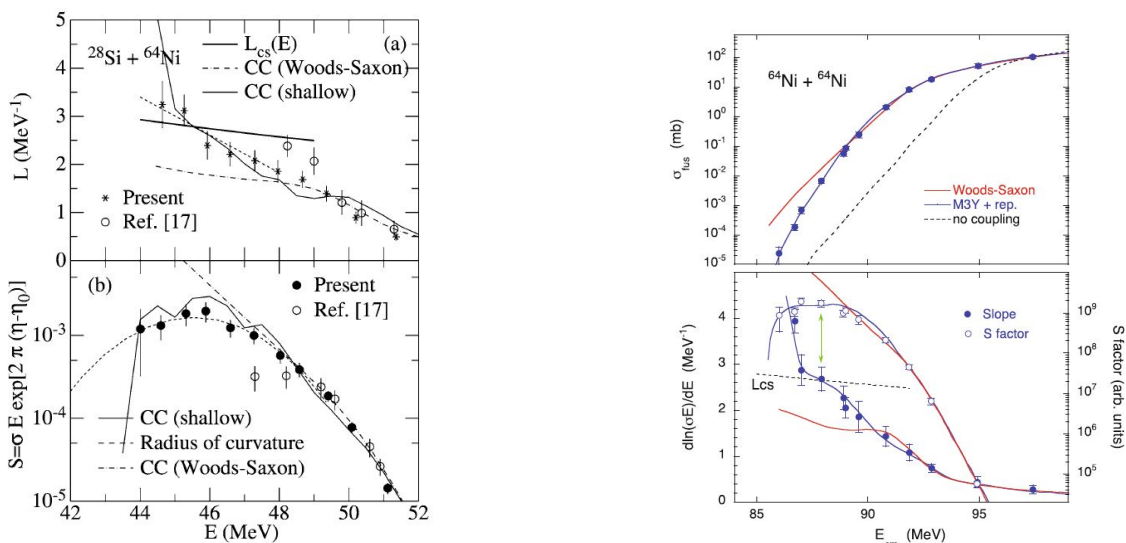
(a) Data plot of $L(E)$ and $S(E)$ for ^{28}Si+^{64}Ni: the S factor maximum is clearly visible and occurs when L reaches L_{CS}, as expected. Note that the factor η is normalized by a constant η_0. Taken from ref. [13].

(b) Excitation function, $L(E)$ and $S(E)$ for ^{64}Ni + ^{64}Ni. One can see that hindrance starts becoming significant at approximately the same energy at which S factor maximum occurs. Taken from ref. [8].
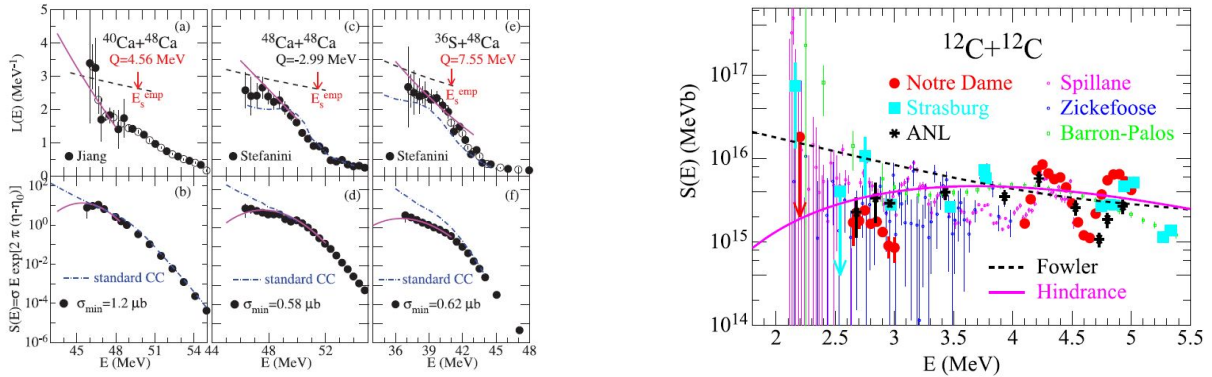
Figure 7

A further clarification is necessary. In systems with negative fusion Q value, $\sigma_{fus}(E)$ (and consequently $S(E)$) must drop to 0 at $E = -Q$, so the presence of an S factor maximum for these reactions is necessary [3][8]. Obviously, that isn't the case for lighter, positive Q value systems: this makes trickier to predict whether hindrance occurs, its energy threshold and its magnitude.

1.4 The case of medium-light systems

Lighter systems exhibit a wider variety of behaviours, as anticipated above, compared to the heavy ones. One important aspect, for example, is the angle at which $L(E)$ crosses the curve representing L_{CS} (condition (24)): experiments have shown that this angle gets smaller going towards light systems, thus "broadening" the $S(E)$ maximum [14], sometimes up to the point that it becomes asymptotic-like.

In addition to this, their experimental analysis presents more difficulties: resonance structures, quasi-molecular excitations and low level densities [14] are just some of the aspects that cause the measured $L(E)$ and $S(E)$ of those reactions, for ex. $^{12}C + ^{12}C$, $^{12}C + ^{14}N$ or $^{16}O + ^{16}O$, to be irregular and to have considerable uncertainties.

Other, more practical, obstacles include the necessity to scan larger scattering angles (for heavy ions, detection is performed near 0° because of the narrower ER angular distribution) and to extend the studied energy range down to hardly-accessible regions.

(a) Various phenomenology of $S(E)$ and $L(E)$ in different medium-light systems. Taken from ref. [14].

(b) Irregular behaviour of $S(E)$ for $^{12}C + ^{12}C$, measured in different researches. Taken from ref. [14].

Figure 8

A feasible solution is to study slightly heavier ("medium-light") nuclei, in order to get rid of the majority of these issues while, at the same time, collecting useful information about astrophysically interesting ones. That's what the research at LNL has been all about in the last years: reactions like $^{12}C + ^{30}Si$ and $^{12}C + ^{24}Mg$ were performed [15][16], seeking fusion hindrance with the aim of improving the current systematics. In this way, it will be hopefully possible to indirectly predict the properties of light systems.
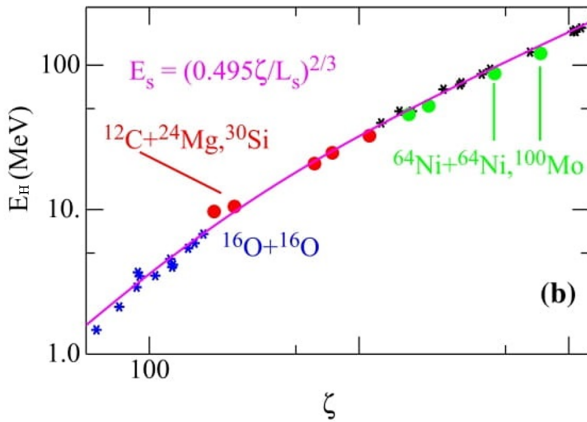

Figure 9: Systematics of S-maximum energy vs $\zeta = Z_1 Z_2 \mu^{\frac{1}{2}}$ for several systems. E_H of the reactions of astrophysical interest, like $^{12}C + ^{12}C$ and $^{16}O + ^{16}O$, can be obtained by extrapolation, using the phenomenological fitting function in magenta, where $L_S = 2.19 + 511/\zeta$. Taken from [3].

The analysis of the reaction $^{12}C + ^{26}Mg$, object of this thesis, is the continuation of this long work.

1.4.1 Motivation for the choice of $^{12}C + ^{26}Mg$

This system was chosen by virtue of ^{26}Mg intermediate properties, between ^{30}Si and ^{24}Mg, already studied.

In the previous research, the reaction involving the latter showed the largest σ_{fus} at hindrance threshold E_H ever measured, among the reactions where an S factor maximum exists [16][17]. In contrast, the measure involving the first one obtained a corresponding cross section about 10 times smaller [15][17], in spite of the proximity of the two systems. A possible explanation involves the different structure of each of them: ^{24}Mg has an alpha-like structure and is deformed (prolate), while ^{30}Si has none of these features [17]. The nucleus of ^{26}Mg, instead, is prolate but not alpha-like, thus making the measurement of its fusion excitation function an optimal test for deducing the reason why such a high cross section is observed at hindrance threshold in the case of ^{24}Mg.

2 The experiment

2.1 Description

Fusion reaction has been obtained by accelerating ^{26}Mg ions through the XTU Tandem electrostatic accelerator, and making them collide with ^{12}C target in a reaction chamber.

If nuclei bind together, they form a compound nucleus (^{38}Ar), which usually de-excites through emission of particles (alphas, neutrons...) and gamma rays. Different less-excited nuclei are produced (see Table 1): these are called *evaporation residues* or ER. These are, in fact, the only possible de-excitation channels for ^{38}Ar, since it is still a quite light nucleus: fission of the compound nucleus has a negligible probability. Thus, by measuring the cross section for ER formation, σ_{fus} is directly obtained.

The importance of an accurate measurement of ER is the reason behind the choice of the *inverse kinematics* collision: by accelerating the heavier nucleus, more kinetic energy of CM is available and the evaporated particles will be faster after evaporation, which makes them easier to detect.

Since most of ER are emitted at very forward angles, i.e. $\theta_{ER} \sim 0°$, it's necessary to separate them from the transmitted beam, and only at this point they can be effectively detected. This is the job of the "Pisolo" deflector+telescope system: the first stage separates ER from beam, and the second measures energy and time of flight of the particles.

2.2 The set-up

2.2.1 Reaction chamber

The chamber where fusion takes place is a cylindrical steel structure, at the end of the beam line coming from the Tandem. Here, the target system is an adjustable vertical ladder, where five targets and a quartz are mounted: the latter emits light when hit by the beam, and is used for beam focusing. For this experiment, the target was $50 \, \mu g/cm^2$ thick, 99.9% enriched ^{12}C foil (no backing necessary). Right behind it, four Si detectors were installed at $\theta = 16°$ with respect to the beam direction in a radial position, each one having a surface of $50 \, mm^2$ (the solid angle is $\Delta\Omega_{mon} = (0.166 \pm 1\%) \, msr$ overall): they are used to measure Rutherford scattering cross section σ_R, which serves as normalization for σ_{fus} (more details in Data Analysis, Sect. 3).

The beam energy range used in the experiment goes from $E_{lab} = 25.5 \, MeV$ up to $50 \, MeV$.

To reach the target optimally, the beam is calibrated both in direction and focus, by modulation of magnetic fields from, respectively, dipoles and quadrupoles installed along the beam line.

2.3 Pisolo setup

As anticipated before, a problem arises when detecting fusion evaporation residues: the residual beam and ER have overlapping directions. An hypothetical direct measurement would be impossible, because the large quantity of beam events detected would cover the ER in the detection. The problem is solved with an electrostatic deflector, which bends the trajectory of ER and beam differently, separating them and making the ER detection possible.

After this "filter", particles enter the actual detector telescope: it consists of two Micro Channel Plate (MCP) detectors, providing fast time signals, a ionization chamber, which measures particle's energy loss, and a silicon detector at the very end, which collects the remaining energy of the ER and acts as a trigger (start) for the acquisition of all signals.

The whole setup is able to rotate around the reaction chamber to obtain the ER angular distribution.

2.3.1 Electrostatic deflector

The deflector is designed to separate the beam nuclei from the ER, using their different electric rigidity. This method was preferred to deflection in a magnetic field, by evaluating the difference

between electric and magnetic rigidity of beam and ER:

$$E\rho = \frac{mv^2}{eq} \qquad B\rho = \frac{mv}{eq} \tag{25}$$

where m is the particle's mass, v its velocity, q its charge number, e is the elementary charge, E and B are the field magnitudes, and ρ is the turn radius (it is not a formal definition for $\overline{E}$).

Here's an example: at $E_{CM} \approx 10\,MeV$, typical quantities are $v_P = 1.59\,cm/ns$ and $\langle q \rangle_P \approx 9.1$ for ^{26}Mg projectile (beam), $v_C = 1.08\,cm/ns$ and $\langle q \rangle_C \approx 10.5$ for a typical ER ^{37}Ar. Both parameters account for in-target energy loss and ionization. From (25):

$$\rho_P(B) \approx 0.47/B\ m \quad \rho_C(B) \approx 0.39/B\ m \quad \rho_P(E) \approx 7.5{\scriptstyle 10^6}/E\ m \quad \rho_C(E) \approx 4.3{\scriptstyle 10^6}/E\ m \tag{26}$$

So, the ratios between the turning radii of beam and ER are ~ 1.2 for $\overline{B}$ deflection and ~ 1.8 for $\overline{E}$ deflection: in spite of the low energy (and thus velocity), the advantage of using an electric field is already evident. The quadratic *vs* linear dependences on v will enlarge the difference even more at higher E. Similar results can be obtained with the other ER species.

Calculations of projectile and ER parameters are made using the software `reaction`, described in Section 2.5.2.

In Pisolo setup, separation is achieved using two pairs of parallel metal plates at high voltage. Between them, a uniform $\overline{E}$ is created: by finely tuning its intensity, the optimal deflection and transmission are obtained. In the best conditions, ER enter the telescope through a collimator, while the beam is stopped against a tantalum plate on the side.
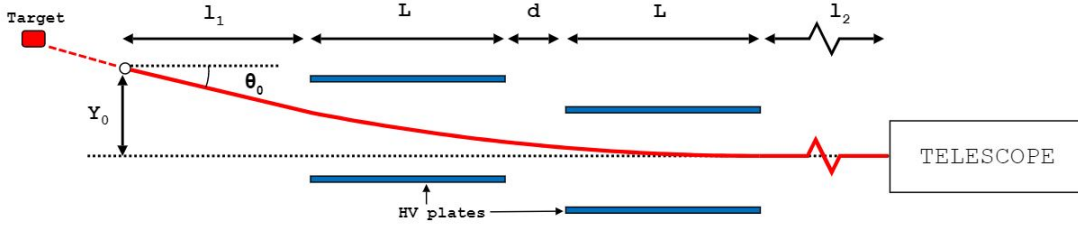

Figure 10: Deflector schematics: $Y_0 = 4.7\,cm$, $\theta_0 = 4.7°$, L = 25 cm, $l_1 = 30\,cm$, $l_2 = 80\,cm$, d = 7 cm, the white dot represents the entrance collimator. The figure doesn't maintain proportions for spacing reasons.

Calculations for optimal $\overline{E}$ intensity are performed numerically, using the software `Maiale.cpp` (more in Sect. 2.5.4).

However, not all beam nuclei are stopped: despite the rejection rate of $\sim 10^{7\text{-}8}$, they constitute part of the noise in the detectors. That's why ToF+E measurements are necessary for a further discrimination.
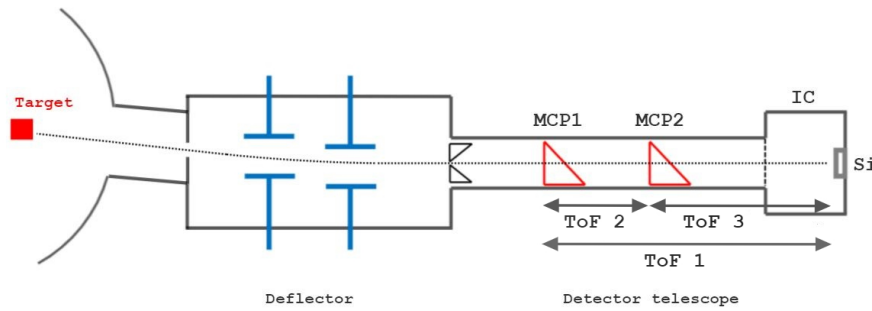
2.3.2 Detector telescope

Figure 11: Pisolo schematics from above.

- **MCP 1 and 2** These detectors have 4 main elements: a $20\,\mu g/cm^2$ thin carbon foil, an electrostatic mirror, a pair of micro-channel plates and a delay line anode. When a charged particle crosses the foil, several electrons are emitted. Those electrons are accelerated by a first electric field, and then a second one deflects them by $90°$. Then they enter the actual MCP, where they're multiplied by a factor of about 10^6. Finally, multiplied electrons are detected by the delay-line grid, a time signal is generated and sent to the electronics. This kind of detector is able to measure also the x-y position of the incident particles, but in this experiment this information is not necessary.
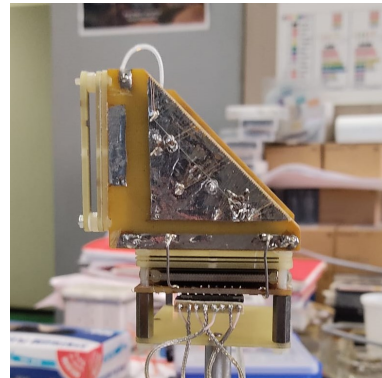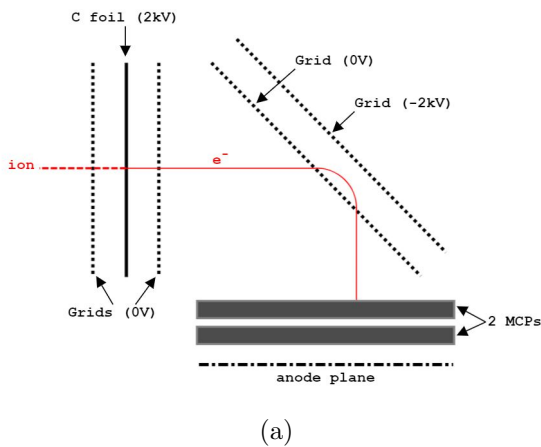

Figure 12: MCP detector and electrostatic mirror schematics and real object.

- **Ionization chamber** The IC is a transverse-field detector and a Frisch grid is placed in front of the anode. The filling gas is methane at low pressure ($10\,mbar$), which is ionized when crossed by a charged particle, as it loses some kinetic energy. The signal produced by the electrons is collected by the anode, and it is proportional to ion energy loss.

- **Silicon detector** It's the last stage of the detection telescope, and its surface determines the total scanned solid angle ($600\,mm^2$, $\Delta\Omega = (0.0357\pm1\%)\,msr$). It collects the particle at the end of the IC, and generates an electric signal due to the induced ionization in its depletion region (in reverse polarization). This signal is proportional to the residual energy of the particle. A trigger signal is also produced, allowing the acquisition of all signals.

The measured quantities are:

- **ToF 1** time of flight between MCP1 and Si final detector.

- **ToF 2** time of flight between MCP1 and MCP2.

- **ToF 3** time of flight between MCP2 and Si final detector (only two of the three ToFs are independent).

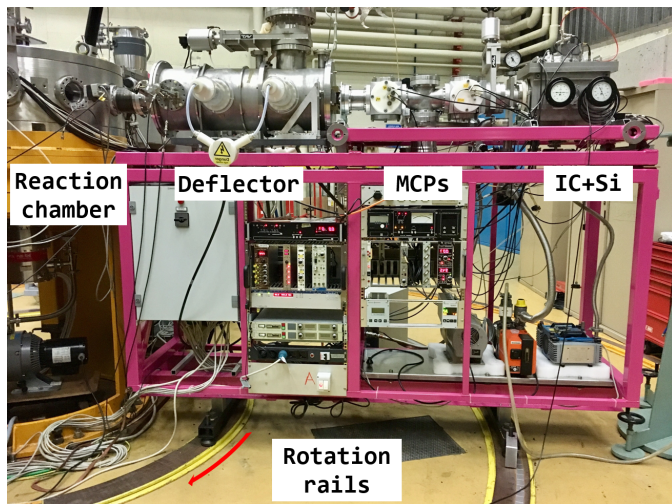- **Total kinetic energy** sum of the energies left by the particle in the IC and Si detector.

Figure 13: The whole setup.

2.4 Vacuum system

The setup described before operates in high vacuum conditions. To achieve this, both reaction chamber and telescope (and obviously the beam pipe coming from the Tandem) are equipped with a set of turbo-molecular and cryo-pumps, fundamental to reach $P \approx 10^{-6}$ mb necessary for the experiment. Turbo-molecular pumps implement a turbine that can rotate at a tangential velocity close to the mean thermal velocity of the pumped gas: through impact with turbine blades, gas molecules are sent out of the vacuum region, and then ejected in the outer atmosphere by a secondary mechanical pump. Cryo-pumps, instead, use helium from a refrigerator device to cool down a portion of vacuum chamber's wall ("cold head"). Here, gas molecules condense and remain located on the surface, thus no longer being part of the internal atmosphere. The latter pumps are used to further lower the pressure.

2.5 Preliminary calculations

Numerical simulations have been performed for evaluation of expected cross section and ER angular distribution, electrostatic deflector calibration and beam energy loss in the target.

2.5.1 Prediction of fusion cross section: `CCfull`

`CCfull` is a free access FORTRAN77 program, developed by K. Hagino, N. Rowley and A.T. Kruppa, which performs Coupled Channels model calculations with all order couplings for heavy ion fusion reactions. The version used here includes the possibility of different target and projectile excitations. The input includes the necessary information about nuclear structure, excitation modes and ion-ion potential, and the program calculates fusion cross section σ_{fus} in the chosen energy range.

[From http://www2.yukawa.kyoto-u.ac.jp/~kouichi.hagino/ccfull.html]

No-coupling excitation function

As first step, simple ion-ion potential calculations (no couplings) are performed, in order to obtain a preliminary excitation function. Being a prior-to-experiment simulation, it only aims to give an idea of the expected measurements. The parameters used are:

- **Wood-Saxon potential:** $V_0 = 40.5$ MeV, $r_0 = 1.10$ fm, $a_0 = 0.6$ fm, taken from a previous similar experiment (^{24}Mg + ^{12}C) [16].

- **Stepping:** $E \in [8; 20]\,\mathrm{MeV}$, $dE = 0.25\,\mathrm{MeV}$.

<table>
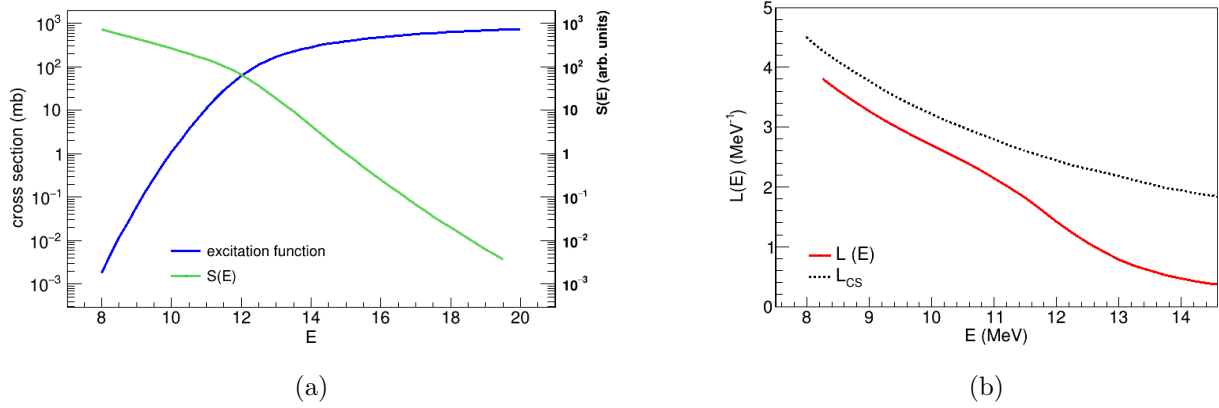<tr><td>(a)</td><td>(b)</td></tr>
</table>

Figure 14: Results of `CCfull` simulation: in the right panel, one can see how $L(E)$ (red line) gets closer to the S factor maximum condition L_{CS} (dashed line), and then remains parallel to it. As expected, then, $S(E)$ keeps increasing (green line, left panel). $L(E)$ is obtained from the excitation function using a finite-differences method.

2.5.2 The `reaction` code

The interaction of beam and ER with the target material determines the energy and the charge state of the outgoing particles. These quantities are obtained with the FORTRAN77 code `reaction`, that implements simple kinematics energy and loss calculations, starting from beam energy, material, density and angle of target and detection angle. Between the various output parameters, the ones used for this experiment are energy loss, straggling, average exit energy and velocity and exit charge state distribution, for both beam and ER.

Expected parameters for outgoing particles

For $E_{lab} = 32\,MeV$ ($E_{CM} = 10.1\,MeV$), using as target $50\,\mu g/cm^2$ ^{12}C foil perpendicular to beam direction, the results, considering the production of ^{37}Ar ER, are:

- **beam**: $\Delta E_{loss} = 0.76\,MeV$, $\langle E \rangle = (31.24 \pm 0.05)\,MeV$, $\langle v \rangle = (1.5232 \pm 0.0013)\,cm/ns$, ToF1 in Pisolo telescope $ToF = 227.8\,ns$, $\langle Q \rangle = 8.97$.

- **ER**: $\Delta E_{loss} = 1.27\,MeV$, $\langle E \rangle = (20.4 \pm 1.3)\,MeV$, $\langle v \rangle = (1.032 \pm 0.033)\,cm/ns$, ToF1 in Pisolo telescope $ToF = 336.1\,ns$, $\langle Q \rangle = 10.21$.

Charge distributions:

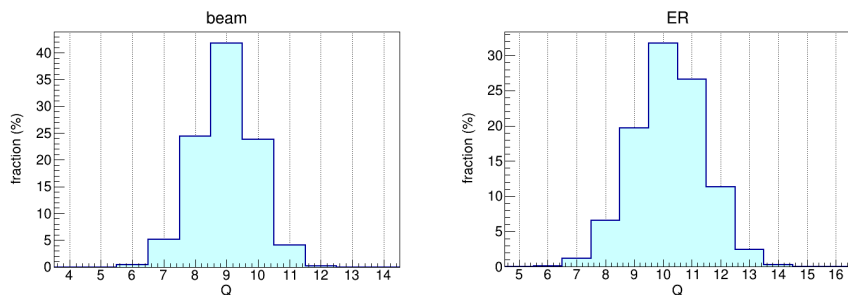Figure 15: Charge distributions for beam and ER (^{37}Ar).

2.5.3 Prediction of ER angular distribution: `PACE4`

`PACE4` is a free access C++ program, available as part of the `LISE++` nuclear spectrometry package. This code performs fusion evaporation simulations through Monte Carlo methods, giving as output a detailed analysis of reaction products: compound nucleus energy, cross sections for every reaction

channel, angular distribution of the different by-product particles and gamma emission are some of the evaluated quantities. Here it's mainly used to obtain total ER angular distribution, needed for σ_{fus} normalization (see Data Analysis, Sect. 3).

The input is given through a graphic interface and includes: basic features of target and projectile nuclei (Z,A, spin), beam initial energy and beam energy loss in the target, potential parameters for each particle species p, n, α and for the incoming channel (these can be automatically taken from systematics) and other minor fine-tuning quantities.

[From https://lise.nscl.msu.edu/lise.html]

ER angular distribution at $\mathbf{E_{lab} = 43.5\,MeV}$ ($\mathbf{E_{CM} = 13.6\,MeV}$)

Before measuring in the low energy region, an angular scan at above-barrier E_{CM} is performed: it's useful to check if the angular distribution presents anomalies and to get the normalization needed to obtain total σ_{fus} from the differential $\frac{\partial \sigma}{\partial \Omega}$.
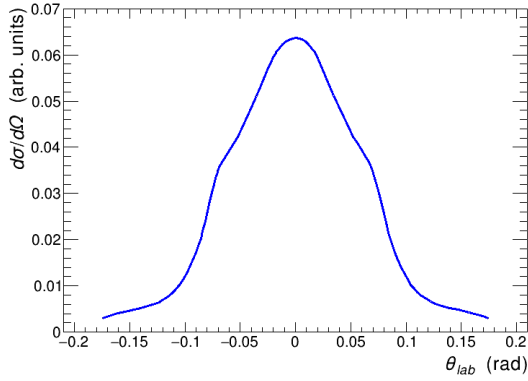

Figure 16: Predicted angular distribution at $E_{lab} = 43.5\,MeV$.

Yields at $\mathbf{E_{lab} = 32\,MeV}$ ($\mathbf{E_{CM} = 10.1\,MeV}$)

For this calculation, projectile and target are considered at spin $S = 0$ and $\Delta E_{loss}(beam) = 0.76\,MeV$ from 2.5.2 is used. Other parameters are automatically set from systematics.

Z	N	A		%	σ (mb)
18	19	37	Ar	30.3%	2.77
17	20	37	Cl	20.8%	1.90
18	18	36	Ar	0.2%	0.0183
17	19	36	Cl	10.7%	0.977
16	18	34	S	10.6%	0.968
16	17	33	S	24.9%	2.27
15	18	33	P	2.5%	0.228

Table 1: Yields of residual nuclei at $E_{lab} = 32\,MeV$.

2.5.4 Electrostatic deflector calibration: `Maiale.cpp`

Since all Pisolo setup relies on the idea of electric rigidity discrimination, numerical simulation of ER trajectory is implemented through `Maiale.cpp`: it's a C++ program (translated from FORTRAN77) developed at LNL for the electrostatic deflector set-up. It takes as input all the geometry parameters of the deflector, ER energy and charge state, and it returns the necessary electric field to correctly bend the particle towards the collimator. It's also possible, by providing the field as input, to obtain the trajectory plot or a set of trajectories for different energies or charge states.

Deflector trajectories

Using the parameters calculated in 2.5.2 ($E_{lab} = 32\,MeV$), particles' trajectories inside the deflector can be simulated. At first, the two electrical fields are tuned for an "average" ER particle: using $\langle Q \rangle_{ER} = 10.21$ and $\langle E \rangle_{ER} = 20.42\,MeV$, optimum values are $E_1 = 7.07\,kV/cm$ and $E_2 = 6.02\,kV/cm$. Then, it's possible to compute how particles (both ER and beam) of different charge and energy behave if those fields are applied.

In the left panel, charge values are fixed to their mean values ($\langle Q \rangle_{ER} = 10.21$ and $\langle Q \rangle_{beam} = 8.97$) and energies are stepped in the ranges $E_{ER} \in [19.1; 21.7]\,MeV$ and $E_{beam} \in [31.2; 31.3]\,MeV$ (the uncertainty ranges of their mean values).

Vice versa for the right panel: fixed energies $E_{ER} = 20.42\,MeV$ and $E_{beam} = 31.24\,MeV$, stepped charge $Q_{ER} \in [7; 13]\,MeV$ and $Q_{beam} \in [7; 11]\,MeV$

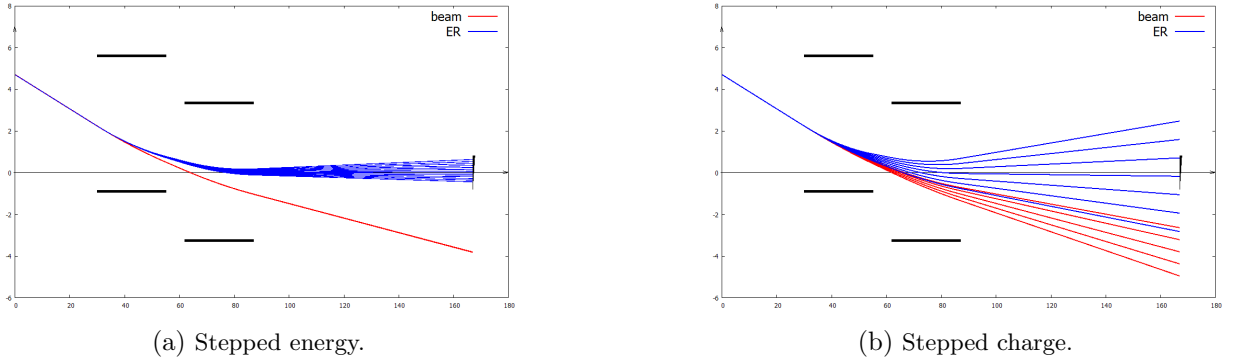(a) Stepped energy.

(b) Stepped charge.

Figure 17

During deflector calibration, predicted electric field values have been used as starting point: optimal values have been chosen by maximization of particles count rate during the experiment. At $E_{lab} = 32\,MeV$, a $\Delta V = 34.24\,kV$ has been applied to both couples of plates, with inter-plate distances of $d_1 = 64\,mm$ and $d_2 = 68\,mm$: that means $E_1 = 5.35\,kV/cm$ and $E_2 = 5.04\,kV/cm$. The necessity of lower values is justified by the fact that the electric field extends also outside the plate region, whereas the simulation only considers an ideal situation of confined fields.

3   Data analysis and results

Data have been collected through more than a hundred runs, with beam energies from $50\,MeV$ down to $25.5\,MeV$ and angle of detection of $2°$, $3°$ and $4°$ (depending on the level of background). About 80 of them were selected for analysis. As anticipated, for each run collected data are:

- Event counts of the four Si monitors at $16°$.
- Three ToFs from MCP detectors.
- IC energy loss (ΔE).
- ER energy collected by final Si detector (E_{Si}).

Usually, the last three are organized in two-dimensional histograms, sometimes called *matrices*, the most useful being the $ToF\,vs\,E_{Si}$.

The analysis is made using `CERN ROOT 6.24` software.

3.1 Cross section formula

The formula used to obtain differential cross section from data is:

$$\frac{d\sigma_{fus}}{d\Omega}(E) = \frac{N_{ER}}{N_{mon}} \cdot \frac{\Delta\Omega_{mon}}{\Delta\Omega_{fus}^g} \cdot \frac{d\sigma_R}{d\Omega}(E) \cdot \frac{1}{T_d \cdot T_{MCP} \cdot T_{IC}} \qquad (27)$$

where N_{ER} and N_{mon} are the number of detected ER and Rutherford events, $\Delta\Omega_{mon} = (0.166 \pm 1\%)\,msr$ is the total solid angle of the four monitors, $\Delta\Omega_{fus}^g = (0.0357 \pm 1\%)\,msr$ is the geometrical solid angle of the final Si detector, $d\sigma_R/d\Omega(E)$ is the Rutherford differential cross section at $\theta_{lab} = 16°$, $T_d = (0.82\pm1\%)$ $T_{MCP} = (0.726\pm0.5\%)$ $T_{IC} = (0.80\pm1\%)$ are the estimated transmission coefficients of the electrostatic deflector, MCP grids and mesh holding the IC window, respectively.

The Rutherford cross section in the laboratory frame can be obtained using the formula:

$$\frac{d\sigma_R}{d\Omega}(E) = \left(\frac{Z_P Z_T e^2}{16\pi\epsilon_0 E_{lab}}\right)^2 \left[\frac{1}{sin^4(\theta_{lab}/2)} - 2\left(\frac{M_P}{M_T}\right)^2 + \left(\frac{M_P}{M_T}\right)^4\right]\,mb/sr \qquad (28)$$

Total fusion cross section is then obtained as

$$\sigma_{fus}(E) = \int \frac{d\sigma_{fus}}{d\Omega}(E)\,d\Omega \qquad (29)$$

This is done by measuring the angular distribution of ER at a given energy (here $E_{lab} = 43.5\,,36.5\,MeV$), and integrating it in the solid angle. Assuming that the shape of the angular distribution is weakly dependent on energy, we can obtain the total cross section at a given energy $\tilde{E}$ by rescaling $\sigma_{fus}(E_{lab} = 43.5\,/36.5\,MeV)$ by the value of measured $d\sigma_{fus}/d\Omega(\tilde{E})$:

$$\sigma_{fus}(\tilde{E}) = \sigma_{fus}(E_{lab} = 43.5\,MeV) \cdot \frac{d\sigma_{fus}/d\Omega\,(\tilde{E}, \theta_{lab})}{d\sigma_{fus}/d\Omega\,(E_{lab} = 43.5\,MeV, \theta_{lab})} \qquad (30)$$

3.2 Examples of analysis

3.2.1 High energy run: $E_{lab} = 43.5\,MeV$

The first information to be extracted is the number of collected Rutherford scattering events. This is done by integrating the corresponding histogram in an energy range containing the main peak, given by beam scattering on ^{12}C, and the smaller sub-peaks, given by beam scattering on other heavier elements, like target impurities or aluminium structure. This procedure is the same for all runs, and an example is given in fig. 18a.

Then the number of ER events is calculated. In the $ToF\,vs\,E_{Si}$ matrices, events form a horizontal parabolic shape, that follows the relationship $E = \frac{1}{2}mv^2 \propto (ToF^{-1})^2$: particles of different mass will group in separate parabolas, as one can see in fig. 18b. The bigger, denser one is made up by beam-like particles that are not completely rejected, while the smaller group underneath represents heavier nuclear species, which are recognised as fusion ER. Those events are selected through a "cut", and the the 2D histogram is integrated inside this area (red polygon in figure).
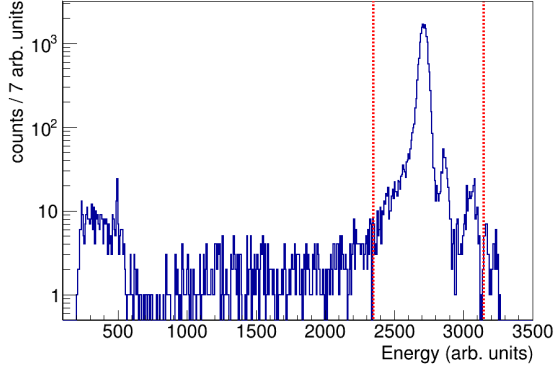
(a) Rutherford scattering energy spectrum: note the log-arithmic y axis.
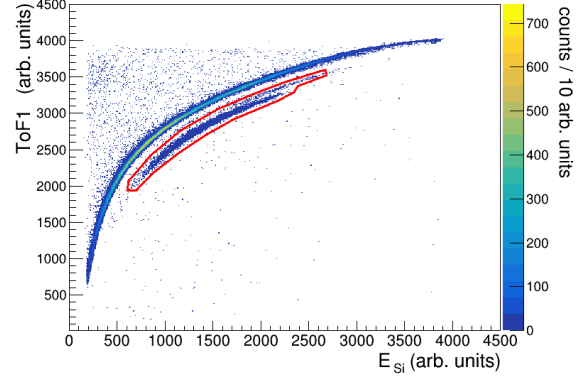
(b) $ToF1\,vs\,E_{Si}$ matrix. Fusion residues are selected with the red polygon. One can see a smaller parabola just above the main ER group: it is made up by a slightly lighter ER specie, that still constitutes a valid signal.

Figure 18

For this run, $N_{mon} = (76610 \pm 280(0.4\%))$ and $N_{ER} = (7406 \pm 86(1\%))$, where statistical uncertainties come from the Poisson-like nature of the event detection.
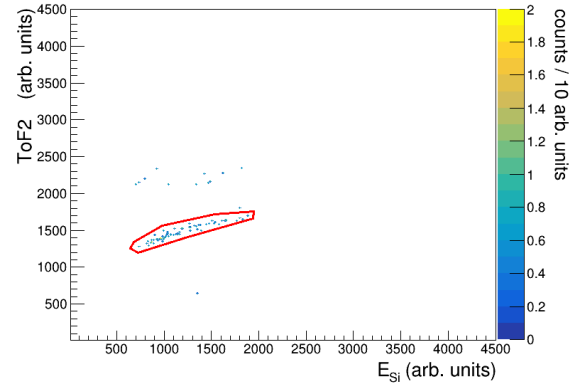
The obtained total cross section is $\sigma_{fus}(E_{lab} = 43.5\,MeV) = (267 \pm 15)\,mb$.

3.2.2 Low energy run: $E_{lab} = 29.0\,MeV$

When measuring at low energy, the ER mass parabola starts to fade and the signal-to-noise ratio decreases. As one can see in fig. 19a, the "signal area" is barely distinguishable from the surrounding background events, and the selection is less accurate. To improve the false-signal rejection, events undergo another selection using the matrix $ToF2\,vs\,E_{Si}$. Here only events from the previous cut are accepted: the separation between ER and beam is now much clearer, as shown in fig. 19b, and a second selection is performed.
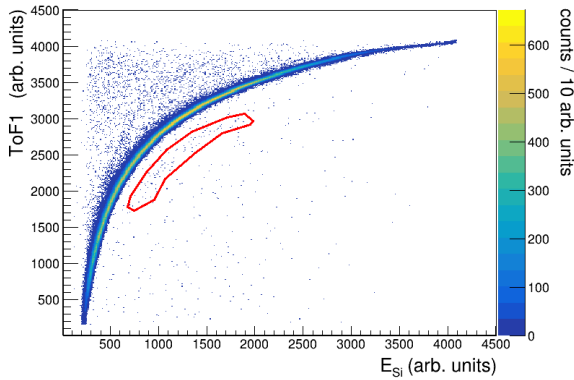
(a) $ToF1\,vs\,E_{Si}$ matrix. The cut here is quite inclusive, and a simple integration would lead to an overestimation of ER counts.

(b) $ToF2\,vs\,E_{Si}$ matrix. By performing a conditional plot (only the events selected in the previous matrix), an accurate selection is possible.

Figure 19

For this run, $N_{mon} = (2.2606 \pm 0.0015(0.07\%)) \cdot 10^6$ and $N_{ER} = (64 \pm 8(13\%))$.

The obtained total cross section is $\sigma_{fus}(E_{lab} = 29.0\,MeV) = (0.207 \pm 0.028)\,mb$.

3.3 Angular distribution

The angular distribution of ER was measured at $E_{lab} = 43.5\,MeV$ at angles $\theta_{lab} \in [-6°, 9°]$, and at $E_{lab} = 36.5\,MeV$ at angles $\theta_{lab} \in [-8°, 8°]$. Data were fitted with an empirical function (sum of two gaussians) as in fig. 20a. Total cross section was computed as integral of the fit function from $43.5\,MeV$ distribution, due to the more accurate fit. The comparison with PACE4 simulation is also excellent. The distribution at $36.5\,MeV$ is instead affected by higher background, but it is useful to check the hypothesis of weak energy dependence of the distribution shape (which is reproduced quite well, see fig. 20b).
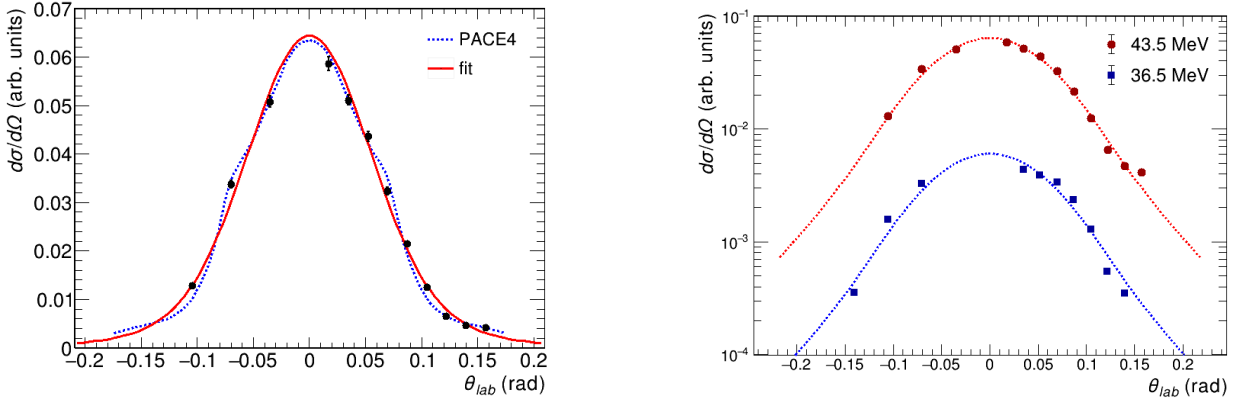
(a) Angular distribution at $E_{lab} = 43.5\,MeV$. Fit has $\chi^2/NDF = 106/10$, which is high but justifiable considering that the distribution is not meant to be exactly gaussian.

(b) Comparison between angular distributions at $43.5\,MeV$ and $36.5\,MeV$. The second one is rescaled by a constant for graphical reasons. Note the logarithmic y axis.

Figure 20

3.4 Results

After data processing, 23 clean points have been adopted for the excitation function. They are compared to the CCFULL predictions, both with and without coupling effects. In both of them, Wood-Saxon parameters are chosen in order to fit the higher energy points: $V_0 = -43.5\,MeV$, $r_0 = 1.10\,fm$ and $a = 0.60\,fm$ are used. The "no coupling" calculation is the result of one dimensional tunneling through the potential; the "coupling" one includes the effects of rotational coupling of levels 2^+ ($E = 1.809\,MeV$ $\beta = 0.482$) and 3^- ($E = 6.876\,MeV$ $\beta = 0.214$) of ^{26}Mg (^{12}C is considered inert), where β is the quadrupole deformation parameter of the nucleus in the corresponding state.
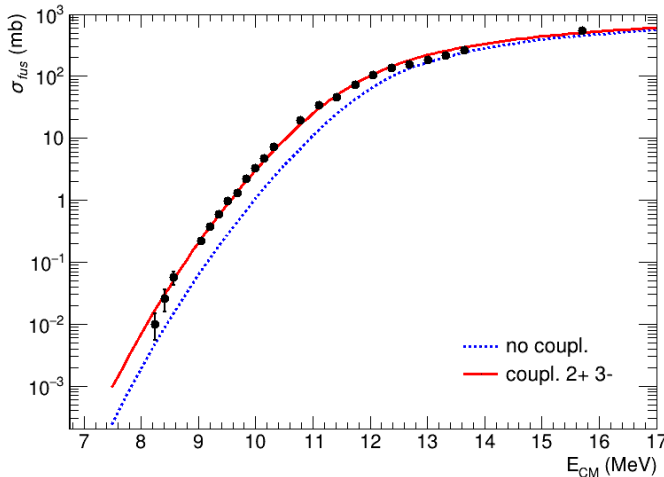

Figure 21: Excitation function for ^{12}C + ^{26}Mg. The two predictions are similar at higher energies, then separate at about $E_{CM} = 12\,MeV$. As expected, a slope change happens at about barrier energy ($11.3\,MeV$) because of the tunneling becoming predominant. The calculations nicely reproduce the data until the last two points, when the cross section seems to drop.

As one can see in the previous figure, the "coupling" calculation fits the data very well, especially at near-barrier energies. The presence of fusion enhancement is quite significant, with a cross section 3-4 times greater than the no-coupling prediction. At energies below $8.5\,MeV$, the excitation function starts decreasing faster than expected, with the last point ($8.25\,MeV$) being incompatible with the prediction. At sub-barrier energies, $S(E)$ and $L(E)$ are computed in order to better understand this behaviour. As shown in fig. 22, in the same energy region of the cross section drop the logarithmic derivative $L(E)$ deviates from the prediction and crosses the L_{CS} curve, although the large uncertainty does not allow to make a safe claim. As expected, then, the astrophysical S factor seems to show a maximum at about the energy where the L_{CS} value is overcome. Just as before, the error bars are quite wide to exclude the possibility of the absence of a maximum.
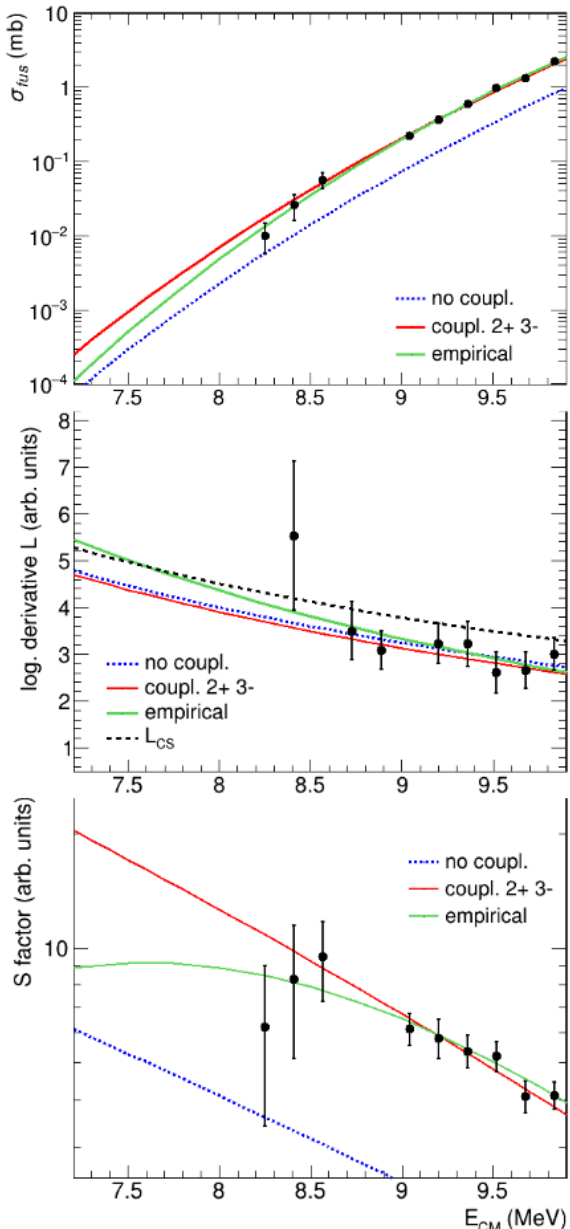

Figure 22: Excitation function, logarithmic derivative and S factor at deep sub-barrier energies. Empirical fit of σ_{fus} and L give respectively $\chi^2/NDF = 3.6/10$ and $4.0/10$.

An empirical fit is performed, using an *a posteriori* hindrance model function from [16]. At low energy, the logarithmic derivative of some light systems follows the empirical formula:

$$L(E) = A_0 + B_0 E^{-3/2} \qquad (31)$$

where A_0 and B_0 are fit parameters. From this, corresponding cross section is calculated:

$$\sigma_{fus}(E) = \frac{\sigma_H E_H}{E} exp\left[A_0(E - E_H) - \frac{2B_0}{\sqrt{E_H}}\left(\sqrt{\frac{E_H}{E}} - 1\right)\right] \quad (32)$$

where E_H ad σ_H are energy and cross section at S factor maximum. $L(E)$ was fitted using (31), in order to find A_0 and B_0, obtaining $A_0 = (-2.0 \pm 0.8)\,MeV^{-1}$ and $B_0 = (140 \pm 30)\,MeV^{1/2}$. Then the parameters are used in (32) to fit the last points of the excitation function. That gives an approximate value of $E_H = (7.6 \pm 0.2)\,MeV$.

What these graphics suggest is that the system is likely to be close to the hindrance threshold, but has not reached it yet. The empirical fit shows the possibility of the presence of an S factor maximum at about $7.6\,MeV$. This fit is made upon the assumption that this reaction behaves like other medium-light systems studied in the past: this hypothesis is reasonable, considering that the empirical model reproduces the excitation function quite well; however, the large uncertainties in the last points (especially of $S(E)$ and $L(E)$) make it difficult to say whether the lowest-energies trend is correctly reproduced. To obtain a strong proof, measurements down to 7-$7.5\,MeV$ have to be performed, possibly with narrower energy steps (so that the uncertainties on $L(E)$ are smaller). At present, the only reasonable claim is that there's a weak evidence of hindrance, with an indication of $E_H \approx 7.6\,MeV$ for the hindrance threshold (and an upper limit of $8.4\,MeV$, corresponding to the lowest point at less than 1σ from CC calculation). A comparison with the present systematics (fig. 9, Section 1.4) seems to confirm this idea, since it provides an expected $E_H = 7.8\,MeV$.

4 Summary and conclusions

In this thesis, the fusion reaction ^{12}C + ^{26}Mg has been studied, describing the experimental work with the Pisolo setup and analizing the obtained data. The experiment consisted in detecting the fusion evaporation residues at forward emission angles, in order to obtain the total cross section of the reaction. In the analysis, the excitation function $\sigma_{fus}(E)$, its logarithmic derivative $L(E)$ and the astrophysical S factor $S(E)$ were compared to the Coupled Channels predictions, in which the coupling of 2^+ and 3^- levels of ^{26}Mg were considered, looking for clues of the hindrance phenomenon.

What emerges from data analysis is a weak evidence of fusion hindrance at energies below $E_{CM} = 8.4\,MeV$. A strong claim is not possible, due to the absence of a clearly defined S factor maximum. Anyway, a fit with an empirical hindrance model suggests the presence of the hindrance threshold nearby, predicting the existence of an $S(E)$ maximum at about $7.6\,MeV$, approx. $0.6\,MeV$ lower than the last measured point. Further data down to $\sim 7\,MeV$ could verify whether the empirical model successfully describes the lowest-energies trend of this reaction and could make a stronger claim about the presence of hindrance. So, from these results it is only possible to give an indication of $E_H = (7.6 \pm 0.2)\,MeV$ (from the empirical fit - the uncertainty is not representative of the confidence level since there are no data points in that region) for the hindrance threshold energy, and to put an upper limit at $E_H^{max} = 8.4\,MeV$, corresponding to the point where the S factor starts deviating by more than 1σ from the CC model. These conclusions agree quite well with the current systematics, that predicts an $S(E)$ maximum at $E_{CM} = 7.8\,MeV$.

Comparing the present results with the closest system already measured, ^{12}C + ^{24}Mg [16], some qualitative clues can be obtained about the influence of the different nuclear structures on fusion dynamics (as anticipated in Sect. 1.4.1). For ^{12}C + ^{24}Mg, hindrance threshold was measured at around $E_H = 0.85V_b$, where V_b is the barrier height, while here the indication is $E_H = 0.67V_b'$, with an estimated cross section at threshold almost 10^3 times smaller than the one of ^{24}Mg. These results may seem unexpected, especially considering the fact that the first 2^+ state of ^{24}Mg is at lower energy ($E = 1.368\,MeV$) and has a greater coupling strength than the 2^+ of ^{26}Mg: at first sight, this should lead to a longer persistence of enhancement, and consequently a lower E_H, in ^{24}Mg. Since both nuclei have a similar static deformation (prolate), the most realistic reason of this difference is rather the alpha-like nature of ^{24}Mg. At present, however, a fusion dynamics model that includes the effects of alpha clustering does not exist, so it is not possible to verify the hypothesis above in this work.

Finally, the indication for E_H can be added to the existing S factor maximum systematics to make a comparison. As said above, there's a good agreement with the empirical extrapolation, and having another data point (although approximated) close to the ^{12}C+^{12}C and ^{16}O+^{16}O systems may reinforce the confidence on the empirical predictions about those astrophysically interesting reactions.
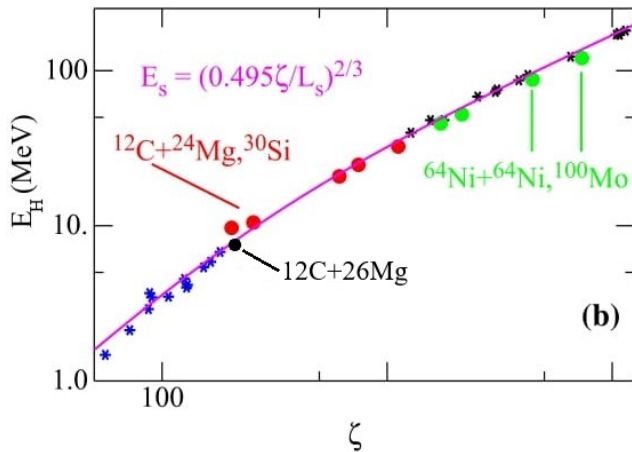

Figure 23: The same systematics of Sect. 1.4, where the present result has been added.

5 Appendix

E_{CM} (MeV)	σ_{fus} (mb)	E_{CM} (MeV)	σ_{fus} (mb)
8.25	0.0101 ± 0.0045	10.79	19.3 ± 1.2
8.41	0.0258 ± 0.0099	11.11	34.0 ± 2.0
8.57	0.056 ± 0.013	11.42	45.6 ± 2.8
9.04	0.220 ± 0.021	11.74	74.0 ± 4.2
9.20	0.369 ± 0.043	12.06	105.1 ± 6.0
9.36	0.593 ± 0.058	12.37	135.0 ± 5.7
9.52	0.987 ± 0.091	12.69	153.4 ± 8.9
9.68	1.31 ± 0.13	13.01	182 ± 10
9.84	2.22 ± 0.18	13.33	214 ± 12
10.00	3.29 ± 0.17	13.64	267.3 ± 7.7
10.15	4.80 ± 0.35	15.70	535 ± 22
10.31	7.21 ± 0.48		

Table 2: Data points of the excitation function.

θ_{lab} (deg)	θ_{lab} (rad)	$d\sigma_{fus}/d\Omega$ (au)	θ_{lab} (deg)	θ_{lab} (rad)	$d\sigma_{fus}/d\Omega$ (au)
-6	-0.1047	0.01281 ± 0.00037	4	0.0698	0.03232 ± 0.00088
-4	-0.0698	0.03370 ± 0.00093	5	0.0873	0.02146 ± 0.00065
-2	-0.0349	0.0508 ± 0.0014	6	0.1047	0.01246 ± 0.00037
1	0.0175	0.0587 ± 0.0016	7	0.1222	0.00651 ± 0.00024
2	0.0349	0.0511 ± 0.0012	8	0.1396	0.00471 ± 0.00017
3	0.0524	0.0436 ± 0.0012	9	0.1571	0.00413 ± 0.00018

Table 3: Data points of the ER angular distribution at $43.5\,MeV$. They are obtained as $N_{ER}/N_{mon} \cdot E_{lab}^{-2}$. To obtain the measurements in mb/sr one should multiply them by the remaining factors of cross section formula (27). Uncertainties already account for the errors in the transmission parameters.

θ_{lab} (deg)	θ_{lab} (rad)	$d\sigma_{fus}/d\Omega$ (au)	θ_{lab} (deg)	θ_{lab} (rad)	$d\sigma_{fus}/d\Omega$ (au)
-8	-0.1396	$7.07 \pm 0.55 \cdot 10^{-7}$	4	0.0698	$6.66 \pm 0.24 \cdot 10^{-6}$
-6	-0.1047	$3.15 \pm 0.13 \cdot 10^{-6}$	5	0.0873	$4.65 \pm 0.16 \cdot 10^{-6}$
-4	-0.0698	$6.49 \pm 0.27 \cdot 10^{-6}$	6	0.1047	$2.57 \pm 0.11 \cdot 10^{-6}$
2	0.0349	$8.72 \pm 0.29 \cdot 10^{-6}$	7	0.1222	$1.08 \pm 0.066 \cdot 10^{-6}$
3	0.0524	$7.82 \pm 0.27 \cdot 10^{-6}$	8	0.1396	$6.96 \pm 0.49 \cdot 10^{-6}$

Table 4: Data points of the ER angular distribution at $36.5\,MeV$.

References

[1] K. Hagino, N. Takigawa, Progress of Theoretical Physics, Vol. 128, No. 6, 2012, p. 1061.

[2] K. Hagino, Lecture at Tohoku University (`nucl.phys.tohoku.ac.jp/~hagino`), Japan.

[3] C. L. Jiang, B. B. Back, K. E. Rehm, K. Hagino, G. Montagnoli, A. M. Stefanini, Eur. Phys. Journ. A, Vol. 57, 2021, p. 235.

[4] P. E. Hodgson, Lecture at Specialist's Meeting, Paris, 13-15 Nov. 1996.

[5] K. Hagino, EPJ Web of Conferences 163, 2017, p. 00022.

[6] V. Zagrebaev, Lecture Notes in Physics 963, pp. 99-120.

[7] D. L. Hill, J. A. Wheeler, Phys. Rev., Vol. 89, No 5, 1953, pp. 1102-1145.

[8] G. Montagnoli, A. M. Stefanini, Eur. Phys. Journ. A, Vol. 53, 2017, p. 169.

[9] K. Hagino, N. Rowley, A. T. Kruppa, Computer Physics Communications, Vol. 123, 1999, pp. 143-152.

[10] M. Dasgupta, D. J. Hinde, N. Rowley, A. M. Stefanini, Ann. Review of Nuclear and Particle Science, Vol. 48, 1998, pp. 401-461.

[11] C. L. Jiang, H. Esbensen, K. E. Rehm, B. B. Back, R. V. Janssens, J. A. Caggiano et al., Physical Rev. Lett., Vol. 89, No 5, 2002, p. 052701.

[12] K. Hagino, A. B. Balantekin, N.W. Lwin, Ei Shwe Zin Thein, Phys. Rev. C, 97, No 3, 2018, p. 034623.

[13] C.L. Jiang, B.B. Back, H. Esbensen, Physics Letters B, Vol. 640, 2006, pp.18–22.

[14] C.L. Jiang, EPJ Web of Conferences, Vol. 17, 2011, p. 01002.

[15] G. Montagnoli, A. M. Stefanini, C. L. Jiang, K. Hagino, F. Galtarossa, G. Colucci, et al., Phys. Rev. C, Vol. 97, 2018, p. 024610.

[16] G. Montagnoli, A. M. Stefanini, C. L. Jiang, G. Colucci, S. Bottoni, D. Brugnara et al., Phys. Rev. C, Vol. 101, 2018, p. 044608.

[17] M. Del Fabbro, G. Montagnoli, A.M. Stefanini, C.L. Jiang, R. Depalo, S. Bottoni, et al., January 2022.